International Journal of Hydrogen Energy 184 (2025) 151868

Contents lists available at ScienceDirect

International Journal of Hydrogen Energy

journal homepage: www.elsevier.com/locate/he

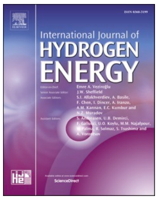

Revealing the Fe doping effect on Ni catalysts for low alkalinity OER: from three-electrode systems to continuous flow anion exchange membrane water electrolyser

David Domingo Huguet [a,b], Víctor Varela-Izquierdo [c], Jaime Cervera Martin [c], Bruno Chaudret [c], Katerina Soulantica [c], Daniel Ruano Sánchez [d], Miriam Díaz de los Bernardos Sanchez [a,*], Cyril Godard [b,**]

[a] Eurecat, Centre Tecnològic de Catalunya, Unitat de Tecnologia Química, C/Marcel·lí Domingo, 2, 43007, Tarragona, Spain
[b] Departament de química física i inorgànica, Universitat Rovira i Virgili, C/ Marcel·lí Domingo 1, 43007, Tarragona, Spain
[c] Laboratoire de Physique et Chimie des Nano-Objets, Université de Toulouse, LPCNO, INSA, UPS, CNRS-UMR5215, 135 Avenue de Rangueil, 31077, Toulouse, France
[d] SRCIT-Universitat Rovira i Virgili, Avinguda Països Catalans 26, Tarragona, 43007, Spain

ARTICLE INFO

Handling Editor: M Mahdi Najafpour

Keywords:
Water electrolysis
OER
Anion exchange membrane
Electrocatalysts
Non-noble-metal

ABSTRACT

Here, we report the use of magnetic induction heating as a rapid and efficient synthesis method to produce Fe@Ni nanoparticles (NPs) with tunable surface coverage and their application as catalysts in the oxygen evolution reaction (OER). This approach enables localized thermal decomposition of precursors, offering improved control over catalyst phase formation. To bridge the gap between lab-scale materials and practical electrolyser integration, the catalysts were deposited onto commercially available Ni-mesh supports suitable for Anion Exchange Membrane Water Electrolyser (AEMWE) operation. The influence of iron content on OER activity was evaluated, and the catalyst performance was validated in a full-cell electrolyser, highlighting the potential of this synthesis route for scalable green hydrogen technologies.

1. Introduction

Over the last decade, electrochemical hydrogen production has gained importance in view of the growing necessity of green and cost-effective technologies for H_2 production [1,2]. Nowadays, two main technologies co-exist at industrial scale for water electrolysis, namely alkaline water electrolysis (AWE) and proton exchange membrane water electrolysis (PEMWE). Alkaline water electrolysis is a mature technology for industrial hydrogen production using well-established Ni-based catalysts that typically have presented low working current densities and inefficient adaptation to incoming electrical current oscillation hindering the total integration of renewable energy suppliers for green hydrogen production [3–6]. Even though advances were achieved in terms of working current density, safety issue concerning gas crossover at low working current densities remains an obstacle that could be efficiently addressed by implementation of the zero-gap cell technologies [7].

On the other hand, proton exchange membrane (PEM) water electrolysis cells use pure water in a zero-gap cell configuration using the proton exchange membrane as solid electrolyte [8]. This zero-gap configuration allows higher current densities with a higher adaptability to incoming current oscillations. Nevertheless, when pure water is used as electrolyte a highly acidic environment is generated at the electrode surface and consequently the process requires the use of very active and corrosion resistance noble metal-based catalysts (*i. e.* Pt, Ir or Ru), thus increasing the overall costs [9–12]. In view of the current advantages and limitations of both technologies (PEM and AWE), anion exchange membrane (AEM) technology has emerged as a combination of both using lower alkaline electrolyte concentration, allowing the use of earth-abundant noble metal free catalysts, and zero gap configuration cell providing higher current densities and higher purity gases [13–16]. Nevertheless, AEM water electrolysis still requires significant

---

* Corresponding author.
** Corresponding author.
E-mail addresses: david.domingo@eurecat.org (D.D. Huguet), varelaiz@insa-toulouse.fr (V. Varela-Izquierdo), cervera-mart@insa-toulouse.fr (J. Cervera Martin), chaudret@insa-toulouse.fr (B. Chaudret), katerina.soulantika@insa-toulouse.fr (K. Soulantica), daniel.ruano@urv.cat (D.R. Sánchez), miriam.diaz@eurecat.org (M.D.B. Sanchez), cyril.godard@urv.cat (C. Godard).

https://doi.org/10.1016/j.ijhydene.2025.151868
Received 29 July 2025; Received in revised form 26 September 2025; Accepted 3 October 2025

improvement in overall process efficiency to become economically viable for industrial implementation. Among the different challenges for efficiency improvement, the principal bottleneck regarding the electrochemical process is the sluggish kinetics of the oxygen evolution reaction (OER).

In alkaline media, the OER is generally described by the adsorbate evolution mechanism, a four-step proton-coupled electron transfer pathway known for its inherently slow kinetics [17–19]. The exact mechanistic route followed during the reaction strongly depends on the structural and compositional features of the catalyst [20–22]. Consequently, synthetic strategies that enable precise control over the composition and surface structure of the electrocatalytically active materials are essential for enhancing OER performance [23,24].

Nickel-based materials are, among others, the most promising anodic catalysts for alkaline OER due to their low cost, moderate catalytic activity, and reasonable stability [19,25–27]. Furthermore, incorporating small amounts of Fe onto Ni-based catalysts was reported to significantly enhance catalytic efficiency [28,29], primarily through the stabilization of the highly active γ-NiOOH phase [30–33]. Several synthetic approaches including hydrothermal synthesis [34], electrodeposition [15,27], solvothermal method [35] and chemical reduction [36] were reported for the preparation of NiFe-based catalysts. These methods typically result in complex surface mixtures of metallic and oxide phases, which complicates the mechanistic interpretation in catalysis. Recent studies described promising OER performances using various NiFe-based nanomaterials. For instance, Fe-doped NiOx particles synthesized via chiral-controlled hydrothermal growth followed by calcination at 550 °C exhibited an overpotential of 340 mV at 10 mA cm^{-2} with a Tafel slope of 49.8 mV dec^{-1} on fluorine-doped tin oxide (FTO) substrates. These materials also demonstrated a low performance of 200 mA cm^{-2} at 1.9 V when tested in a full-cell architecture AEMWE [37]. Similarly, $Ni_{90}Fe_{10}$ alloy NPs produced via Sonic Cluster Beam deposition onto indium tin oxide (ITO) supports showed an overpotential of 320 mV at 1 mA cm^{-2} after optimization of catalyst thickness [38]. Another study reported a material with a similar Ni:Fe ratio synthesized by chemical reduction of metal nitrates on various metal oxide supports, displaying higher overpotentials ranging from 329 to 384 mV at 10 mA cm^{-2}, with Tafel slopes between 65 and 73 mV dec^{-1} [39].

In view of the limitations of classical synthetic methods in terms of surface control and taking advantage of the intrinsic magnetic properties of Ni and Fe, magnetic induction heating emerges as an appealing alternative synthetic route. The thermal decomposition of metallic precursors under an alternating magnetic field can indeed provide localized and controlled heating at material surfaces, potentially offering a more precise strategy for catalyst synthesis [40,41]. Although magnetic induction heating was primarily explored for catalytic applications as a localized energy source [42–44], its potential in materials synthesis remains practically unexplored. In a recent study, Raya-Barón et al. reported the successful synthesis of core–shell nanoparticles via magnetic induction heating, employing a magnetic core as the starting material [45]. Indeed, the use of an external magnetic field have been studied as heating source to locally increase FeNi based electrocatalysts temperature under reaction conditions improving the overall alkaline water electrolysis [46,47]. Nevertheless, stability issues concerning electrocatalytic materials and supporting materials difficult large scale implementation [48].

A major challenge in scaling up nanoparticle-based OER catalysts to practical electrolyser devices lies in their effective integration onto suitable and stable electrical-conductive supports. For lab-scale testing, catalysts are typically deposited onto rigid substrates such as glassy carbon, FTO or metal conducting materials, which are not always compatible with commercial electrolyser architectures and, in some cases lead to data misinterpretation [49,50]. In contrast, full-cell electrolyser configurations—particularly in proton exchange membrane water electrolysers (PEMWE)—rely on membrane electrode assemblies (MEAs) fabricated by spray-coating or casting catalyst inks directly onto polymer membranes like Nafion, which are chemically and mechanically robust under standard processing conditions [51]. For that reason, a full study from three-electrode set up to full-cell architecture devices is mandatory to fully understand a catalysts behaviour and confirm its reliability.

However, this process is more complex for anion exchange membrane water electrolysers (AEMWE), due to the lower thermal and mechanical stability of AEMs, which limits direct coating methods. Consequently, spray-coating catalyst inks onto gas diffusion layers (GDLs) has become the preferred method for AEMWE systems [13,52]. Among the commercially available GDL materials, Ni-foam and Ni-mesh are widely used due to their high electrical conductivity, tailored porosity, and catalytic compatibility. Although Ni-foam offers a large surface area and high porosity, it suffers from poor mechanical resistance under the compressive forces typically applied during electrolyser assembly. Therefore, to ensure mechanical stability and reliable large-scale implementation, Ni-mesh was selected as the support in this study.

In this work, we explore magnetic induction heating as efficient method to synthesize Fe-decorated Ni nanoparticles, namely Fe@NiNPs, for OER catalysis. The impact of Fe surface coverage at different levels on catalytic performance was systematically investigated. Moreover, we demonstrate the practical integration of these catalysts into AEMWE systems using commercially available Ni-mesh supports, with the aim of identifying potential synergistic effects and assessing the viability of this synthesis approach for scalable applications.

2. Experimental section

2.1. Chemicals

Due to the air-sensitivity of the metallic precursors and the produced NPs, the synthesis and the purification of the nanoparticles was performed under inert atmosphere either by using a glove box or by standard Schlenck techniques. $\{Ni[{}^{i}PrNC(CH_3)N^{i}Pr]_2\}$ $(Ni(AMD)_2)$ and $\{Fe[N(SiMe_3)_2]\}_2$ $(Fe_2(HMDS)_4)$ were purchased from NanoMEPS, palmitic acid (PA, ≥99 %) and hexadecylamine (HDA, ≥98 %) were purchased from Sigma-Aldrich, potassium hydroxide (KOH, ≥85 %) was purchased from VWR Chemicals. All reagents were used as received without further purification. Mesitylene (99 %) and Toluene (99 %) were purchased from VWR Prolabo. Solvents for synthesis were used from solvent purification system, degassed by bubbling Ar through the solution for ca. 40 min, dried with activated molecular sieves and stocked in the glovebox. Deionized water used for electrolyte preparation was type I from a MilliQ (Merck Millipore) equipment. Inks were prepared using reagent grade organic solvents, MilliQ water and Nafion 117 resin solution (5 wt %) from Sigma Aldrich as ionomer.

2.2. Nickel nanoparticles (NiNPs) preparation

Nickel nanoparticles were prepared by thermal decomposition of $\{Ni[{}^{i}PrNC(CH_3)N^{i}Pr]_2\}$ $([Ni(AMD)_2])$ organometallic precursor in the presence of H_2. As general procedure, in the interior of a glove box, $[Ni(AMD)_2]$ (342 mg, 1.0 mmol) was dissolved in 4 mL of mesitylene and added in to an 80 mL Fisher-Porter (FP) bottle under magnetic stirring followed by the addition of 422 mg of HDA (422 mg, 1.75 mmol) dissolved in 6 mL of mesitylene. The FP bottle was sealed, transferred to a vacuum line and the purple mixture (10 mL) was then charged with 3 bar of H_2. The decomposition reaction was carried out at 100 °C with magnetic stirring (500 rpm) for 24 h. The FP bottle was then allowed to cool to room temperature. The NiNPs were isolated by magnetic decantation, washed with toluene (3× 5 mL), dried under reduced pressure and stored in the glove box (ca. 60 mg). Bulk chemical composition determined by TGA and ICP-OES analysis included in Table 1. TGA was used in order to determine the total metallic composition of samples regarding the presence of organic moieties from

Table 1
Chemical composition determined by TGA and ICP-OES of the synthesized NPs.

Entry	$\{Fe[N(SiMe_3)_2]_2\}_2$ (mg)	$\{Fe[N(SiMe_3)_2]_2\}_2$ (mmol)	M[a] (wt %)	Ni[b] (wt %)	Fe[b] (wt %)	Ref.
1	–	–	80	94.9	–	NiNPs
2	13.4	0.018	–	91.2	2.5	$Fe_{2.5}$@NiNPs
3	26.9	0.035	–	88.1	5.8	$Fe_{5.8}$@NiNPs
4	53.9	0.072	–	79.2	11.1	Fe_{11}@NiNPs

[a] Measured by TGA.[b]Measured by ICP-OES. *Reaction Conditions*: NiNPs (50.0 mg, 0.85 mmol), $Fe[N(SiMe_3)_2]_2\}_2$ (see Table 1), PA (87.8 mg, 0.35 mmol), H_2 (3 bars), 54.6 mT (300 kHz), 15 h.

stabilizing agent used in NPs synthesis. Final Ni content was determined by ICP-OES analysis as a more specific technic to determine the selective dissolved metals in acidic solution.

2.3. Fe decorated NiNPs preparation: Fe@NiNPs

To study the role of each metal in the reaction, a series of materials based on NiNPs decorated with different ratios of Fe were synthesized (Scheme 1). Prior to the synthesis of Fe@NiNPs, the heating capacity of the NiNPs under an alternating magnetic field (AMF) was assessed using a commercial induction system (Fives Celes, MP12), operating at 300 kHz and generating a root mean square amplitude between 8.5 and 76 mT. The materials were prepared by decomposition of $\{Fe[N(SiMe_3)_2]_2\}_2$ ($[Fe_2(HMDS)_4]$) organometallic precursor in solution in the presence of NiNPs as support and heating agent. As a general procedure, NiNPs (50.0 mg, 0.85 mmol) were introduced in a 100 mL Fischer-Porter bottle (FP) with PA, 87.8 mg, 0.35 mmol) as stabilizing agent, the desired amount of $\{Fe[N(SiMe_3)_2]\}_2$ (see Table 1) and mesitylene (15 mL) as solvent. The decomposition reaction was carried out under 3 bar H_2. The FP was placed in the center of the inductor coil and the desired temperature was obtained by adjusting the power of the AFM to obtain a bulk temperature of ca. 80 °C (measured with an infrared camera at the external reactor wall). The final conditions were set at 54.6 mT with a power of 9.5 kW in a 300 kHz inductor coil. The reaction time was set at 15 h for all the reactions to ensure the total decomposition of the Fe precursor. When the reaction was completed, $Fe_{wt\%}$@NiNPs (wt% = 2.5, 5.8 and 11) were isolated by magnetic decantation, washed with toluene (3x5 mL), dried under reduced pressure and stored in the glove box (ca. 50 mg). All samples were slowly oxidized by air exposure before its use using a vial capped with a septum previously perforated with a needle. Bulk chemical composition determined by TGA and ICP-OES analysis included in Table 1.

2.4. Materials characterization

Thermogravimetric analyses (TGA): Initial metal content of NiNPs was determined by TGA in a TGA/DSC 1 STAR System equipped with an ultra-microbalance UMX5, a gas switch GC200 and DTA and DSC sensors.

Inductively coupled plasma optical emission spectrometry (ICP-OES): The Ni and Fe contents of the materials were measured per duplicate for each sample using ICP-OES (ICAP 6300 Thermo RF Generator with a Polychromator-from 166 to 847 nm with a Charge Injection Device (CID) detector) after digestion in aqua regia at 80 °C for 12 h.

Transmission electron microscopy (TEM): The size and the morphology of the NPs were studied by bright-field TEM (BF-TEM) imaging using a JEOL microscope (Model 1400) working at 120 kV. Additionally, the morphology and metal distribution within the nanoparticle was studied at by high-resolution transmission electron microscopy (HRTEM) observations using a JEOL F200 TEM ColdFEG operated at 200 kV.

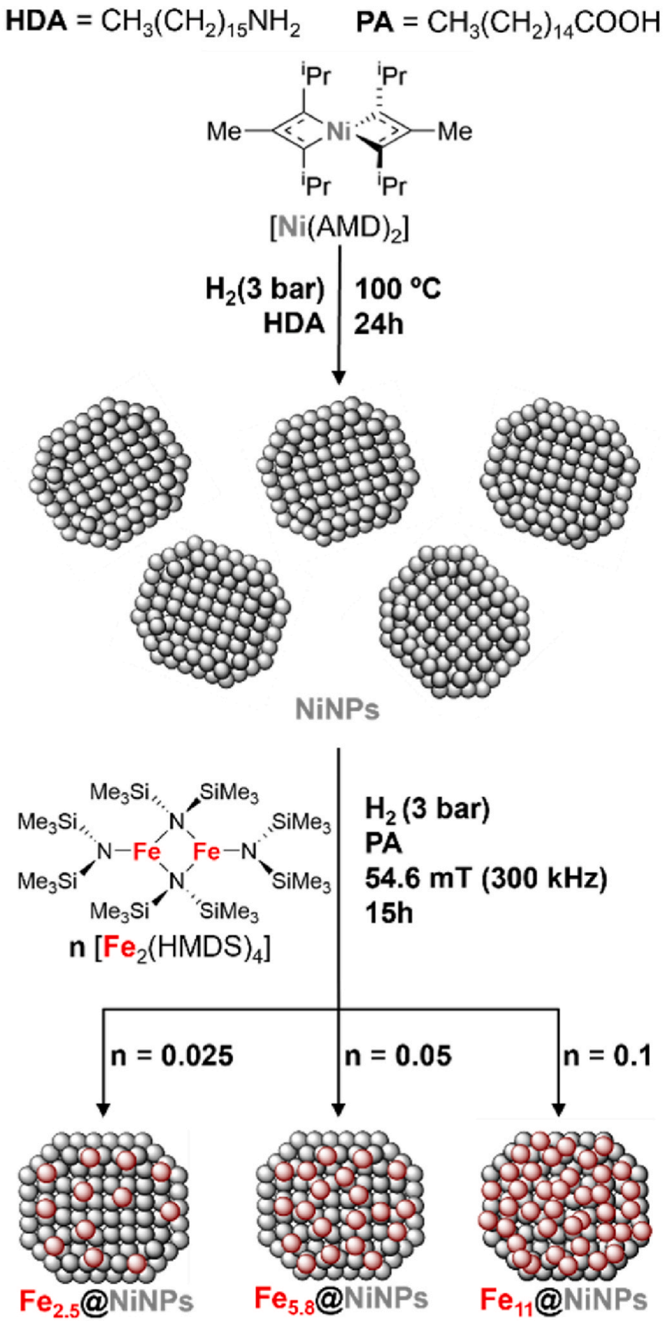

Scheme 1. Schematic representation of NiNPs and $Fe_{wt\%}$@NiNPs preparation.

High-Resolution transmission electron microscopy (HRTEM): HRTEM images were acquired with a Gatan OneView camera, a CMOS-based and optical fibre-coupled detector of 4096 by 4096 pixels. Gatan Digital Micrograph program was used to process the TEM images. STEM images (1024 x 1024 pixels) were recorded from the JEOL bright-field (BF) and high-angle annular dark-field (HAADF) detectors using the Gatan DigiScan3 scanning unit with a camera length of 150 mm. Samples were inserted in a JEOL beryllium double-tilt holder for energy dispersive x-ray spectroscopy (EDS). STEM-EDS mapping was recorded from an EDS Centurio detector (silicon drift) with an effective area of 100 mm^2 and 133 eV of energy resolution. STEM-EDS maps (512 x 512 pixels) were processed with the JEOL Analysis software. In all cases, TEM grids were prepared by depositing one drop of a colloidal solution containing air exposed NPs in toluene on a copper grid covered with amorphous carbon. HR-TEM grids were prepared with the same procedure but using hollow carbon covered copper grids. ImageJ software was used to obtain particle size distributions from the TEM images and thereon analyzed in terms of Gaussian statistics to obtain the mean size and standard deviation parameters.

X-Ray diffraction (XRD): Routine XRD measurements for crystalline phase identification were carried out in reflection geometry on a PANalytical Empyrean diffractometer using Co−Kα radiation (λ = 0.1789 nm), operating at 35 kV and 45 mA. Data were collected over a 2θ range of 30–110°, with a step size of 0.05° and a time per step of 35 ms for a total acquisition time of 56 min. To prevent metal oxidation of the samples containing metallic Fe and Ni, the powder samples were prepared and sealed with Kapton polyimide films in the glovebox. Samples were further studied after air exposure using a Bruker-AXS D8-Advance diffractometer with vertical theta-theta goniometer, incident- and diffracted-beam Soller slits of 2.5°, a fixed 0.5° receiving slit and an automatic Air-scattering knife on the sample surface. The angular 2θ range was between 5° and 110°. The data were collected with an angular step of 0.02° at a step/time of 0.5 s. Cukα radiation was obtained from a copper X-ray tube operated at 40 kV and 40 mA. Diffracted X-rays were detected with a PSD detector LynxEye-XE-T with an opening angle of 2.94°. Sample was deposited on a low-background support (Si (510)). The diffractograms were interpreted with the software DIFFRAC.EVA 6.1 from BRUKER.AXS and the database PDF-2 release 2022 from ICDD (International Center for Diffraction Data). The Rietveld refinement (Rietveld, 1969) [53] was performed with the TOPAS v6 software (Bruker AXS GmbH, 2017), (Coelho, 2018) [54]. The background was modelled with a 2nd order Chebyschev polynomial. The instrumental contribution to the diffraction profile was calculated with the S4 Fundamental Parameters Approach (Cheary, Coelho, & Cline, 2004) [55]. The relative quantitative phase analysis was obtained by refining the Rietveld scale factor for each phase and applying the corresponding well-known equations (Hill & Howard, 1987) [56]. The peak width of each phase was modelled with the Double-Voigt Approach (Balzar, 1999) [57] by considering only the Lorentzian contribution of the crystallite size effect and discarding any contribution of the micro strain to the peak width.

Vibrating-sample magnetometry (VSM): Magnetic characterization was carried out using a physical property measurement system (PPMS, Quantum Design) in the vibrating sample magnetometer configuration (VSM). The sample was prepared inside the glovebox to prevent metal oxidation of the samples containing Ni or Fe as a dry powder (ca. 10 mg) enclosed in a Teflon capsule. The hysteresis loops were measured for magnetization vs magnetic field at 300 and 5 K, using an external field of up to ±3 T.

Specific absorption rate (SAR): SAR was used to determine the heat generation of a material upon exposure to an external magnetic field. SAR values were estimated using calorimetry experiments with a 93 kHz fixed frequency coil, following an optimized protocol described in previous works [58]. In a typical experiment, a glass sample tube was charged with magnetic NPs (10 mg), PA (~0.5 mg) as stabilizing agent to prevent agglomeration and organic solvent (0.5 mL, mesitylene). The magnetic NPs were dispersed in the solvent by sonication for a few seconds after closing the tube inside of the glovebox to prevent NPs oxidation. During the calorimetric experiments, the sample tube was placed in the center of a magnetic coil filled with 1.8 mL of deionized water. Two optic fiber temperature probes were submerged in water, one near the socket's bottom and the other near its center. Then, the increase in temperature after applying an alternating magnetic field for 50 s was measured at different field amplitudes in a 100 kHz inductor coil. The sample was exposed to field amplitudes varying between 0 and 47 mT. After applying a precalculated correction factor that accounts for the heat losses to the surroundings, it was possible to construct a curve of SAR (W g^{-1}) against field amplitude (mT).

X-ray photoelectron spectroscopy (XPS): XPS analysis was performed at SRCiT (URV) using a ProvenX-NAP (Specs Surface Nano Analysis GmbH, Berlin, Germany) spectrometer with a monochromatic X-ray source (μFocus450). The measurements were collected under these conditions: power of X-ray of 100 W (AlKα anode = 1486.7 eV), the hemispherical analyzer operating in the main fixed analyzer transmission mode, entrance slit of 7 × 20 mm and exit slit open with mesh. The beam spot size at sample position was around 200 μm of diameter. The data was recorded with a PHOIBOS 150 NAP 1D-DLD and the total pressure in the main vacuum chamber during the analysis was better than $2 \cdot 10^{-9}$ mbar. Survey spectrum was collected at 80 eV of pass energy and 0.7 eV of step size. To obtain more detailed information about chemical environment and oxidation states, high-resolution spectra were recorded from individual peaks at 30 eV of pass energy and 0.3 eV of step size. Each specimen was analyzed at an emission angle of 0° measured from the surface normal. Assuming typical values for the electron attenuation length of relevant photoelectrons, the XPS analysis depth ranges between 5 and 10 nm for a flat surface. Data processing was performed using CasaXPS processing software version 2.3.26.PR1.0 (Casa Software Ltd., Teignmouth, UK). Binding energies were referenced to the C1s peak at 284.8 eV (adventitious carbon). The Ni $2p_{3/2}$ region was fitted following the methodology described in Biesinger's articles, in which each nickel species is fitted using distinct components [59–63].

2.5. Electrochemical characterization

2.5.1. Rotating disc glassy carbon electrode electrochemical characterization

Basic electrochemical characterization was carried out in a three-electrode cell configuration using a rotating disc electrode (RDE) system (Autolab PGSTAT302 N potentiostat, rotating disc electrode from Autolab (RDE-2)). A Pt-foil (1 cm^2) was used as counter electrode, and Ag/AgCl electrode (3 M KCl) was used as reference. The working electrode was a glassy carbon electrode (GCE) (0.07 cm^2) (Autolab). Prior to catalyst deposition, the GCE was polished sequentially with 0.3 μm and 0.05 μm alumina suspensions (Buehler) on microcloth polishing pads and then cleaned in Milli-Q water using an ultrasonic bath for 30 s. Catalyst ink was prepared by dispersing 2 mg of catalyst powder in 125 μL of an ethanol/water solution (4:1, v/v) followed by the addition of 10 μL of Nafion resin solution (5 wt%). The suspension was sonicated for 30 min in an ultrasonic bath to obtain a homogeneous dispersion. The ink was drop-casted onto the GCE surface (2 μL total volume), resulting in a catalyst loading of 0,42 mg/cm^2. The electrode was dried in a vacuum oven at 40 °C, with gradual increase in vacuum to prevent ink splashing and to facilitate bubble removal, ensuring optimal contact between the catalysts layer and the electrode. The electrode was then immersed in degassed 1 M KOH electrolyte (at room temperature) and let spin for 10 min at 1600 rpm prior to measuring the open circuit potential (OCP), which was recorded for 300 s under static conditions. Subsequently, cyclic voltammetry (CV) was performed in the non-faradaic region (1.0–1.2 V *vs* RHE) at various scan rates (20, 40, 60, 80 and 100 mV/s) to determine the capacitance double layer (C_{dl}) and estimate the electrochemical surface area (ECSA) before and after the activation procedure. Catalyst activation was performed by running CVs between 1.0 V–1.60 V (*vs* RHE) at scan rate of 50 mV/s, until the voltammograms overlapped exactly for at least 50 consecutive cycles (information available in S.I. Section 3). Once a stable response was achieved, a second set of CVs in the non-faradaic region was recorded to determine the post-activation ECSA. Finally, linear sweep voltammetry (LSV) was performed from 1.0 V to 1.70 V (*vs* RHE) at a scan rate of 5 mV/s. All potentials reported in the study were converted from Ag/AgCl [3 M KCl] ($E^{\circ}_{Ag/AgCl}$ = 0.210 V) to RHE scale using the following equation [64]:

$$E(vs.\ RHE) = E(vs.\ Ag\,/\,AgCl) + E^{o}_{Ag/AgCl}(vs.\ RHE) + 0.059 \times pH$$

All measurements were performed in triplicate and without IR compensation.

C_{dl} of the materials was determined from the slope of the linear fit of the capacitive current versus scan rate (see S.I. Section 4)

2.5.2. NiMesh supported materials electrochemical characterization

A commercial nickel mesh (NiMesh, dimensions: 1 cm × 1 cm x 0.25 mm; from TopTitech, China), was used as the working electrode for catalyst stability tests under stress conditions, employing the same potentiostat setup. For these measurements, a Pt gauze counter electrode (0.0762 mm wire diameter, 99.9 % metal basis, 0.53 g, 2.5 × 2.5 cm; Thermo Scientific) was used. Prior to use, the NiMesh was cleaned by sonication in acetone (20 mL, 3 × 10 min) followed by a final sonication step in deionized water (20 mL, 1 × 10 min).

For the preparation of the NiMesh working electrode, 2 mg of catalyst powder were dispersed in a mixture of 700 μL isopropanol, 100 μL water and 10 μL Nafion resin solution (5 wt%). The suspension was sonicated for 30 min in an ultrasonic bath to obtain a homogeneous dispersion and then manually sprayed onto the NiMesh, which was placed on a heating/vacuum table preheated at 90 °C to ensure rapid solvent evaporation.

The prepared electrode was immersed in degassed 1 M KOH electrolyte, which was magnetically stirred prior to the measurement. The open circuit potential (OCP) was recorded for 300 s under static conditions. Catalyst activation was performed by cyclic voltammetry (CV) between 1.0 V and 1.60 V (*vs* RHE) at a scan rate of 50 mV/s until the voltammograms overlapped exactly in successive cycles, indicating electrochemical stabilization of the catalyst layer (information available in S.I. Section 3). Once a stable CV response was achieved, linear sweep voltammetry (LSV) was performed from 1.0 V to 1.70 V (*vs* RHE) at scan rate of 5 mV/s. This was followed by chronoamperometry (CA) at 1.70 V (*vs* RHE) for 6 h to evaluate the catalyst under continuous operation.

2.5.3. Full-cell AEM 5 cm^2 electrolyser tests

The materials were evaluated in a custom-built 5 cm^2 electrolyser cell (a photograph of the setup is provided in Figure S.I. 24). The anode was prepared using the same procedure described for NiMesh supported electrode, employing a 5 cm^2 NiMesh electrode (2.25 × 2.25 cm) with a final catalyst loading of ~1.5 mg. The cathode consisted of a 2.4 × 2.4 cm piece of commercial Pt Black-coated carbon cloth electrode (2 mg/cm^2) purchased from Fuel Cell Store (W1S1011). Different anode and cathode sizes were used to reduce the risk of membrane rupture during operation. A Sustainion X37-50-Grade RT membrane (5 × 5 cm, Dioxide Materials) was used as the anion exchange membrane. It was pre-treated in 1 M KOH solution (in water) for 48 h (according to the stablished protocol [65]). The electrodes and membrane were inserted into PTFE gaskets and assembled between two titanium current collector plates with serpentine flow channels. The full system was closed using stainless steel end plates tightened to 3 Nm torque and equipped with an integrated heating system. Electrical insulation was ensured with silicon gaskets. After assembly, a 15 mL/min flow of 1 M KOH electrolyte was pumped through the bottom inlets of the cell using a dual-channel peristaltic pump, feeding the anode and cathode from separate reservoirs. The electrolyser cell and reservoirs were then heated to 60 °C and maintained at that temperature for 4 h to ensure uniform thermal distribution before electrochemical measurements. A Keysight E36731A battery emulator was used to apply the desired current or voltage. Polarization curves were recorded in galvanostatic mode, starting with an initial 30-min step at 50 mA/cm^2, followed by 5-min steps with incremental increases of 50 mA/cm^2. The cell voltage was reported as the average value over the last 30 s of each step. A cut-off voltage of 2.2 V was set for all experiments. Catalysts stability was assessed by chronoamperometry at a constant cell voltage of 2.0 V for 24, 48 and 72 h, with a polarization curve recorded every 24 h.

3. Results and discussion

3.1. Physical, chemical and magnetic characterization

Monometallic Ni nanoparticles (NiNPs) were prepared by thermal decomposition of $[Ni(AMD)_2]$ under 3 bar H_2 in the presence of HDA as stabilizing agent, at 100 °C for 24 h under vigorous magnetic stirring (see Experimental Section). Transmission electron microscopy (TEM) images revealed a monodisperse particle size distribution with an average size of 5.3 ± 0.6 nm (see Figure S.I. 1). Thermogravimetric analysis (TGA) confirmed a Ni metal content of 80 wt% where the remaining 20 % of the sample weight was assigned to organic content from stabilizing agent. (Table 1). The magnetic properties of the NiNPs were determined by vibrating sample magnetometry (VSM). After confirming their heating capability by SAR measurements, the NiNPs displaying a SAR calorimetry value of 20 W g^{-1} were used both as support and as inductive heating agent for the decomposition of the $[Fe_2(HMDS)_4]$ metallic precursor under 3 bar H_2, in the presence of palmitic acid (PA, 0.5 eq relative to NiNPs) as a stabilizing agent. The reaction was conducted under an AMF of 54.6 mT with a power input of 9.5 kW for 15 h. Three $Fe_{wt\%}$@NiNPs nanomaterials were prepared by varying the Fe concentration in the reaction medium. Inductively coupled plasma (ICP-OES) analysis confirmed Fe loadings of 2.5, 5.8 and 11 wt% on the NiNPs surface (see Scheme 1). TEM analysis of the $Fe_{wt\%}$@NiNPs revealed a progressive increase in particle size with increasing Fe content, with mean diameters of 6.1 ± 0.8 nm, 6.8 ± 1.1 nm and 7.2 ± 0.8 nm (see Fig. 1a–f). Further insights into the surface composition were obtained by high-resolution HRTEM in scanning transmission mode (STEM) coupled with energy-dispersive X-ray spectroscopy (EDS). Elemental mapping revealed partial surface coverage of the Ni core at low Fe content, evolving toward a nearly complete core-shell structure at higher Fe loadings (Fig. 1g–o). Additional characterisation data are provided in Figures S.I. 2 to 7.

Powder XRD mainly revealed the presence of metallic Ni *fcc* structure. No peaks could be assigned to metallic iron, which crystallizes in the *bcc* phase. An alloy can be formed between Ni and Fe in low Fe concentration promoting the stabilization of an *fcc* structure of Fe–Ni as Tetrataenite phase [66](Fig. 2). The $Fe_{wt\%}$@NiNPs were also characterized by XRD after slow air exposure to avoid violent oxidation. The oxidized NPs diffractogram displayed a distortion from the metallic Ni *fcc* structure that was assigned to the formation of a NiO *fcc* Bunsenite phase as a passivation layer that prevents the total oxidation of the metallic Ni core. The incorporation of Fe in the structure reduces the intensity of NiO peaks at 37° indicating a better protection due to surface coverage of the metallic Ni. Moreover, with the sample that contains the highest amount of Fe, Fe_{11}@NiNPs, new peaks corresponding to iron oxide phases were detected. $Fe(OH)_3$ Bernalite phase in very low amounts could be identified among different iron oxide phases (20°–24°) [67] while in lower Fe content samples iron oxide phases cannot be clearly identified mainly due to low concentration and possible amorphous structure. Additional signals present at angles lower than 20° were associated to organic and silicon-based surface contaminants from stabilizing agent and precursor decomposition.

Analysis of the magnetic properties by VSM was performed on the $Fe_{wt\%}$@NiNPs materials and the expected behaviour regarding M_s and H_c values at 5 K was observed due to reported iron higher M_s and lower H_c [41,68–73]. First, NiNPs exhibited ferromagnetic behaviour, with a saturation magnetization value (M_s) of 49 A m^2 kg^{-1} with a coercivity field (H_c) of 52 mT. However, Fe-decorated materials ($Fe_{wt\%}$@NiNPs) showed an increase of M_s compared to NiNPs up to 74 A m^2 kg^{-1} upon the incorporation of Fe onto the material (Fig. 3). Furthermore, a decrease was observed in the H_c 52 mT for NiNPs to 18 mT for Fe_{11}@NiNPs. This trend has also been observed in other FeNi alloys and has been attributed to enhanced interparticle magnetostatic interactions, as reported by Dijith et al. [74]. SAR values for the prepared materials also increased from 20 W g^{-1} for NiNPs to 144 W g^{-1} for Fe_{11}@NiNPs due to the incorporation of a harder magnetic material on the surface of the nanoparticles, which enhanced their overall heating efficiency [75] (Fig. 4).

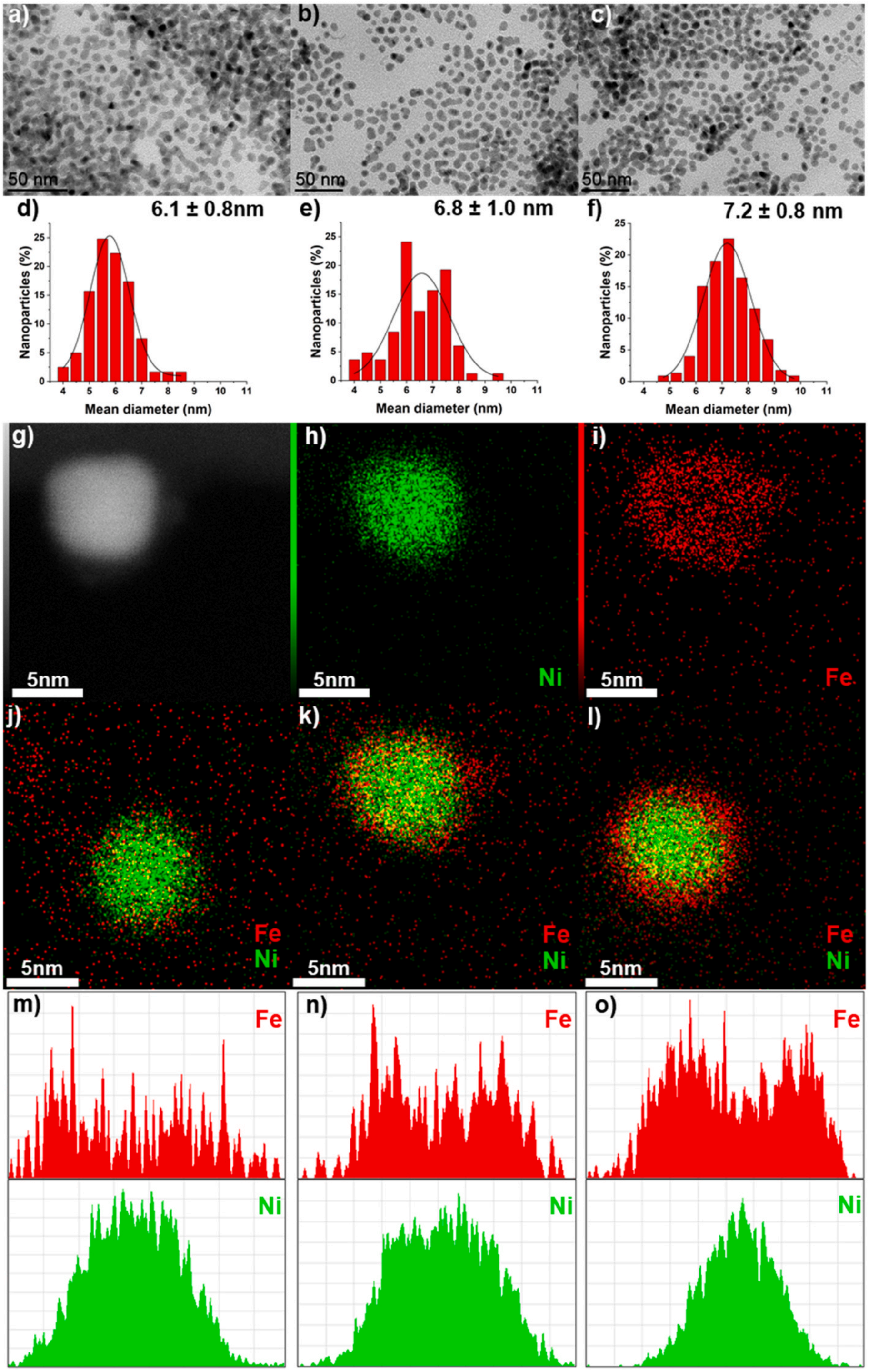

Fig. 1. TEM image of: a) $Fe_{2.5}$@NiNPs, b) $Fe_{5.8}$@NiNPs and c) Fe_{11}@NiNPs. Particle size distribution of: d) $Fe_{2.5}$@NiNPs, e) $Fe_{5.8}$@NiNPs and f) Fe_{11}@NiNPs. g) STEM-HAADF image of an isolated $Fe_{5.8}$@NiNPs. STEM-HAADF-EDS elemental mapping from an isolated $Fe_{5.8}$@NiNPs of h) Nickel (green) and i) Iron (red). STEM-HAADF-EDS elemental mapping overlay of an isolated j) $Fe_{2.5}$@NiNPs, k) $Fe_{5.8}$@NiNPs and l) Fe_{11}@NiNP. Elemental profile distribution of isolated m) $Fe_{2.5}$@NiNPs, n) $Fe_{5.8}$@NiNPs and o) Fe_{11}@NiNPs. (For interpretation of the references to colour in this figure legend, the reader is referred to the Web version of this article.)

3.2. GCE electrochemical characterization

Electrochemical measurements using a glassy carbon electrode (GCE) were performed to evaluate the catalytic activity of the synthesized materials. When the iron-decorated Fe_{11}@NiNPs sample was tested, an overpotential (η) of 396 mV at 10 mA/cm^2 was recorded, along with a Tafel slope of 113 mV/dec. These results were comparable to those obtained with the pure NiNPs (η = 395 mV, Tafel slope of 86 mV/dec), which exhibited an electrochemical surface area (ECSA) of 6.8 cm^2. For the Fe_{11}@NPs, high-resolution transmission electron microcopy (HRTEM) confirmed an almost complete coverage of the Ni core (green) by the Fe shell (red) (Fig. 1 l), consistent with a slightly reduced ECSA value of 5.8 cm^2. In contrast, materials with lower Fe content showed enhanced electrochemical performance. The $Fe_{5.8}$@NiNPs and $Fe_{2.5}$@NiNPs exhibited lower overpotentials of 342 mV and 341 mV, respectively, at 10 mA/cm^2. Regarding the reaction

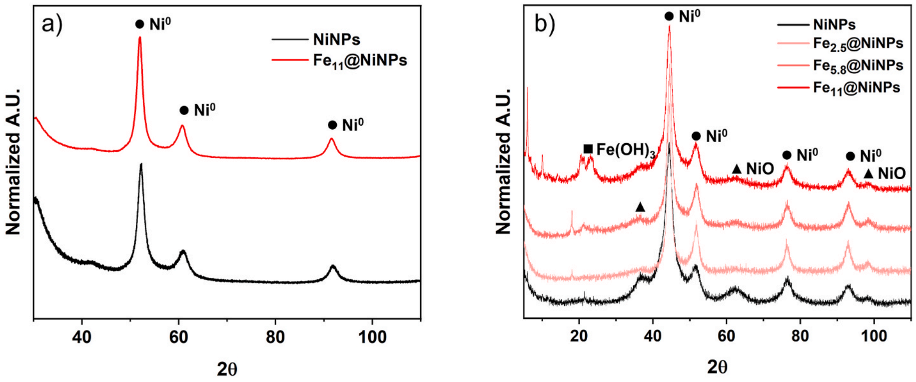

Fig. 2. a) XRD diffractogram of NiNPs and Fe$_{11}$@NiNPs under inert atmosphere, b) XRD diffractogram of NiNPs and Fe$_{wt\%}$@NiNPs after air exposure.

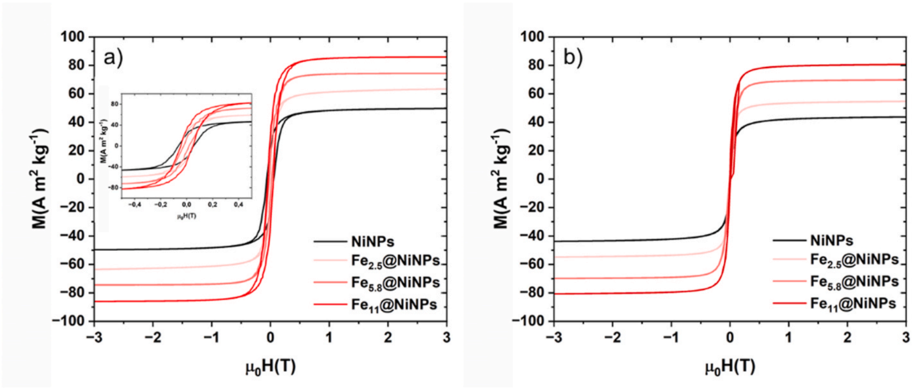

Fig. 3. Hysteresis loop obtained for NiNPs and Fe$_{wt\%}$@NiNPs a) at 5 K, b) at 300 K.

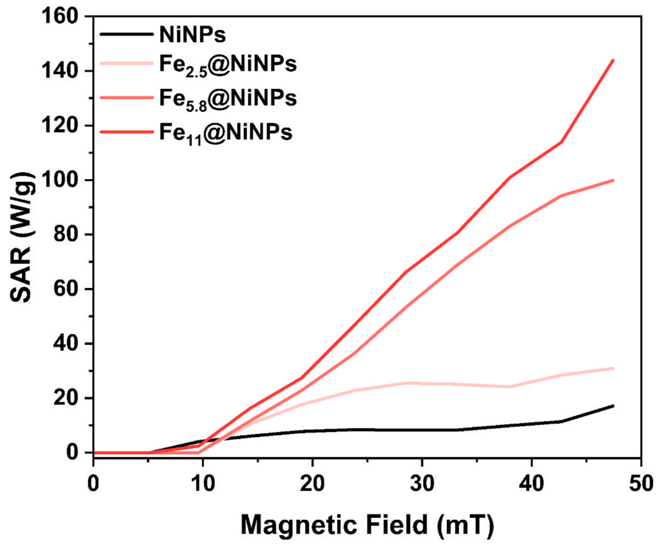

Fig. 4. SAR values obtained for NiNPs and Fe$_{wt\%}$@NiNPs.

kinetics, Tafel slopes of 58 mV/dec (Fe$_{5.8}$@NiNPs) and 70 mV/dec (Fe$_{2.5}$@NiNPs) were determined (Fig. 5). The corresponding ECSA values were 8.7 cm^2 and 5.8 cm^2, respectively (see S.I. Section 4). These results suggest that partial iron coverage enhances the electrochemical performance of Ni-based nanoparticles, likely due to synergistic effects at the Fe–Ni interface that improve both charge transfer and active site accessibility.

To further rationalize this trend, a deeper analysis of the electrochemical surface area (ECSA) and the surface composition of the catalyst was carried out (see S.I. Section 4). This behavior can be attributed to the variation in ECSA at both low and high iron loadings, suggesting that optimal catalytic performance is achieved under a balanced surface composition. In the case of Fe$_{2.5}$@NiNPs, the overall number of active centers is likely limited due to the lower Fe–Ni ratio. Conversely, for Fe$_{11}$@NiNPs, HRTEM combined with EDS mapping revealed extensive iron coverage of the Ni surface, which reduces availability of Ni active centers at the catalyst interface. Additionally, the characteristic anodic peak associated with β-NiOOH formation, typically observed at 1.4 V (*vs* RHE) for pure NiNPs, was shifted to >1.45 V (*vs* RHE) in the Fe$_{wt\%}$@NiNPs samples. This shift indicates the stabilization of higher Ni^{3+} and Ni^{4+} oxidation states in the γ-NiOOH phase, facilitated by the presence of Fe (Fig. 6) [32,37,76,77]. These findings reinforce the key role of Fe in tuning the surface composition and electronic structure of Ni-based electrocatalysts, thereby improving their activity and stability toward the oxygen evolution reaction (OER).

3.3. Ni mesh electrochemical characterization

To better assess the stability and performance of the catalysts under more practical conditions, the materials were deposited onto 1 cm^2 NiMesh electrodes by spray-coating, achieving a final catalyst loading of approximately 1 mg/cm^2. The resulting electrodes, denoted as Fe$_{wt\%}$@NiNPs/NiM, exhibited similar trends to those observed with GCE, but additional synergistic effects arising from interactions with the catalytically active Ni support were identified. The bare NiMesh displayed an overpotential of 448 mV at 10 mA/cm^2, which was significantly reduced to 388 mV upon deposition of NiNPs (NiNPs/NiM). Incorporation of Fe further enhanced the performance, with Fe$_{2.5}$@NiNPs/NiM showing the lowest overpotential 311 mV, followed by Fe$_{5.8}$@NiNPs/NiM (325 mV) and Fe$_{11}$@NiNPs/NiM (330 mV) (Fig. 7 a). A synergistic effect between the Fe$_{wt\%}$@NiNPs and the NiMesh

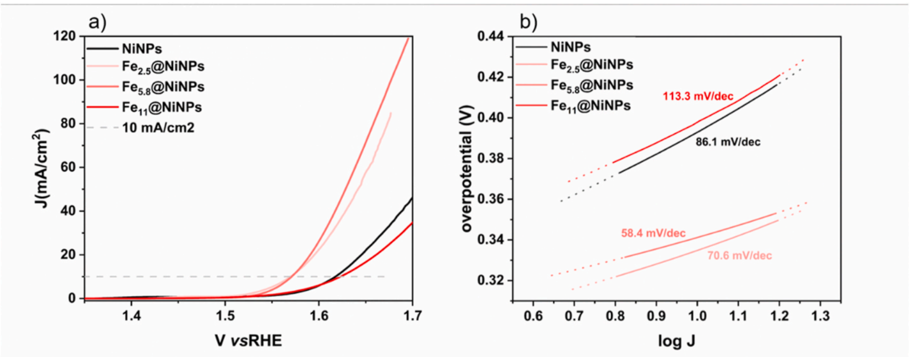

Fig. 5. a) LSV of materials tested in GCE and b) Tafel Plots.

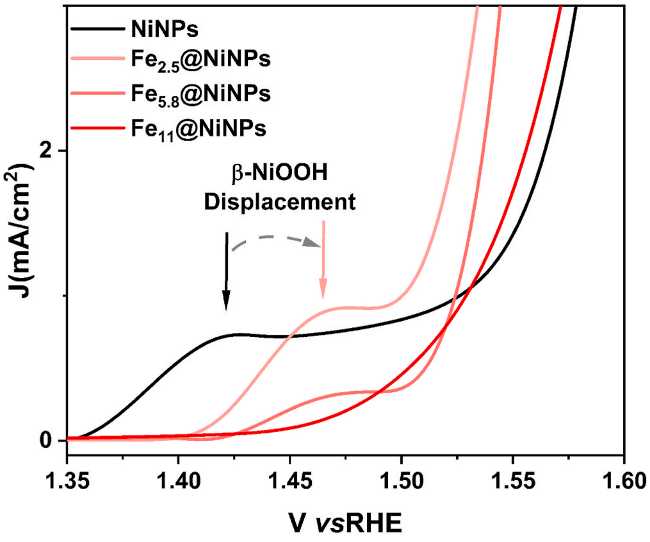

Fig. 6. *LSV magnified for the β-NiOOH region in materials deposited over GCE.*

support is thus evidenced, particularly in the case of Fe_{11}@NiNPs/NiM, which exhibited a lower overpotential than NiNPs/NiM, despite its lower intrinsic activity on GCE. This improvement is likely due to an overall increase of the Ni–Fe interfacial ratio in the system, as the iron-decorated nanoparticles are in direct contact with the NiMesh, further promoting the formation of catalytically active Ni–Fe sites. The reaction kinetics followed a similar trend to that observed on GCE. The Tafel slope for bare NiMesh was 142.6 mV/dec, which decreases to 99.1 mV/dec upon deposition of NiNPs. The Fe-containing samples displayed even lower values, with $Fe_{5.8}$@NiNPs/NiM showing the best performance (83.9 mV/dec), followed by Fe_{11}@NiNPs/NiM (90.8 mV/dec) and $Fe_{2.5}$@NiNPs/NiM (91.6 mV/dec) (Fig. 7 b). The similarity in Tafel slopes among the three Fe-decorated samples further supports the existence of a synergistic effect with the NiMesh substrate, which contributes to enhancing the kinetics of the OER. In addition, a clear change on the 1.4 V vs RHE -1.5 V vs RHE was observed, maintaining the displacement of anodic β-NiOOH formation peak. Nevertheless, in this case this peak displacement can be observed among all the three Fe decorated samples, thus evidencing the synergistic effect generated between the support and the iron-decorated nanoparticles (Fig. 8).

The study of LSV displayed a clear change in the slope observed at potentials above 1.65 V *vs* RHE (Fig. 7 a), indicating a transition from kinetically controlled regime to one limited by mass transport due to product bubble formation observed at electrode surface. To simulate the operating conditions of a practical electrolyser, a short stability test was conducted at 1.7 V (*vs* RHE), within the diffusion-limited region for 6 h. Under these conditions, the recorded current densities can be attributed to differences in product/electrolyte diffusion at high current levels 78, 79. In terms of short-term performance, the NiNPs/NiM catalyst exhibited a minimal current loss of 0.03 mA/h.

For the Fe-decorated samples, current degradation rates increased with iron loading: $Fe_{2.5}$@NiNPs/NiM showed the lowest loss (0.005 mA/h), followed by $Fe_{5.8}$@NiNPs/NiM (0.05 mA/h) and Fe_{11}@NiNPs/NiM (0.11 mA/h) (Fig. 9). These results indicate that electrochemical stability is strongly influenced by the Ni-to-Fe ratio. A higher Ni content appears to suppress Fe leaching by stabilizing iron species within the catalyst structure, an effect that has been previously reported in the literature [80–82]. This preliminary study was performed to determine the most suitable material to be implemented for full-cell architecture AEMWE tests among the prepared materials.

3.4. X-ray photoelectron spectroscopy characterization

Ex situ X-ray photoelectron spectroscopy (XPS) was employed to investigate the surface composition and chemical states of pristine and

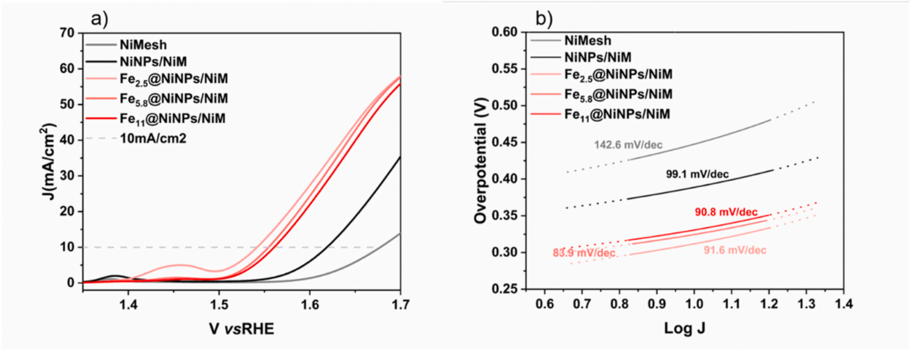

Fig. 7. a) LSV of materials tested in Ni Mesh and b) Tafel Plots.

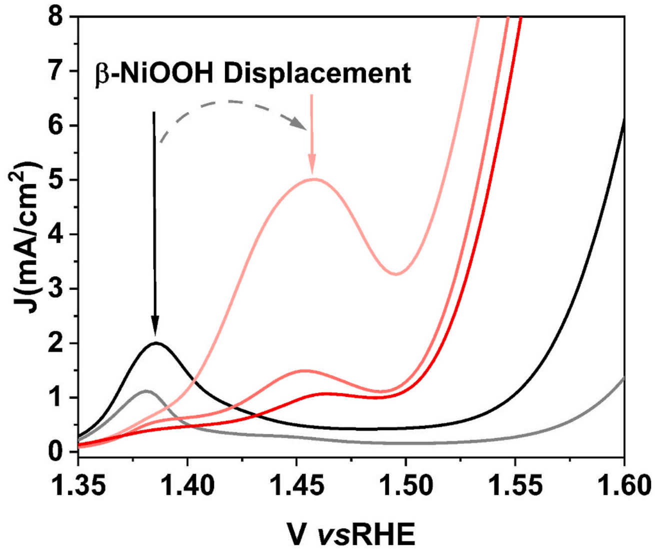

Fig. 8. *LSV magnified for the β-NiOOH region in materials deposited over NiMesh support.*

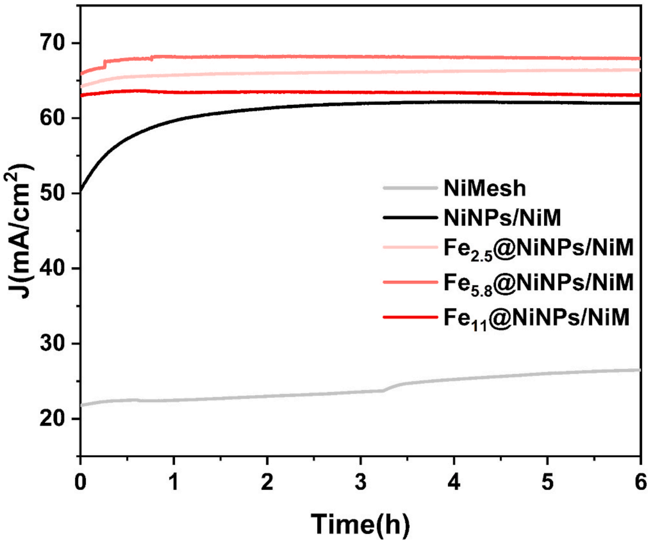

Fig. 9. Chronoamperometry measurements of NiNPs and $Fe_{wt\%}$@NiNPs materials supported in NiMesh.

modified nickel mesh (NiMesh) electrodes. The modifications involved NiNPs deposition (NiNPs/NiM) and Fe incorporation ($Fe_{2.5}$@NiNPs/NiM), using ink formulations without Nafion to eliminate fluorine-related signals. In fluorinated systems, the F 1s region typically exhibits two peaks: one at 684 eV corresponding to metal fluorides, and another at 688 eV, attributed to organic fluorine species [83]. These signals may overlap with Ni LMM Auger peaks (610–650 eV), while the F KLL Auger features at ~832 and ~858 eV can interfere with the Ni $2p_{3/2}$ region (~850–860 eV) [84]. Moreover, the relaxation peak produced from F 1s overlaps with Fe 2p region (~700–740 eV). $Fe_{2.5}$@NiNPs/NiM was selected as studying material due to its lower overpotential among all the materials while having a low surface coverage allowing a proper study of the changes in the Ni species present in the surface of the sample. As visual example, the survey spectra of post catalytic $Fe_{2.5}$@NiNPs/NiM (Fig. 10) reveal characteristic signals for Ni 2p, O 1s, and C 1s present in all samples. A weak Fe 2p signal at ~709 eV was also detected in $Fe_{2.5}$@NiNPs/NiM, confirming Fe incorporation [63]. The C 1s region shows a main peak corresponding to adventitious carbon (284.8 eV) assigned to environmental contamination and a secondary peak 288.5 eV that has been assigned to possible surface organic contamination (O–C=O) of the commercial NiMesh [59,61,85]. For post-catalytic samples two main peaks appear in the same C 1s region at 293.2 eV and 296.3 eV corresponding K $2p_{1/2}$, coming from surface contamination by the KOH electrolyte used [86]. For XPS detailed spectra of all samples see S.I. Section 5.

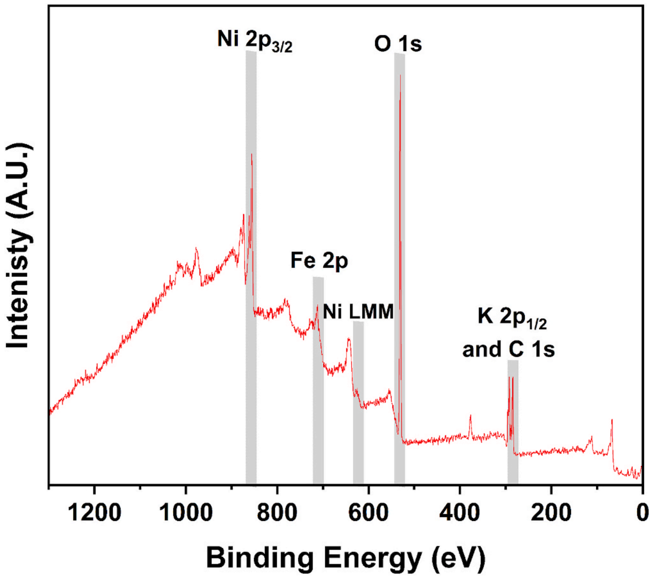

Fig. 10. Survey spectra $Fe_{2.5}$@NiNPs/NiM.

The study of Ni LMM Auger region facilitates the interpretation of Ni $2p_{3/2}$ region identifying the presence of different possible Ni species. A main peak on the Ni LMM Auger region (Fig. 11) was observed at KE = 846 eV. This value of kinetic energy is associated in literature with metallic Ni [87,88]. A signal peak at 832.8 eV of kinetic energy was observed, which can be assigned to γ-NiOOH, as was evident in the pristine NiMesh sample.

In NiNPs/NiM and $Fe_{2.5}$@NiNPs/NiM, an enhancement of a broad peak at KE = 843.9 eV was also observed, indicating a higher proportion of NiO, which partially overlaps with the γ-NiOOH signal. The Ni $2p_{3/2}$ region (Fig. 12a,c,e) further supports these findings. All samples exhibit a metallic Ni peak at BE = 852.6 eV. The broader oxidized Ni envelope was fitted using established fitting parameters, revealing contributions from NiO and γ-NiOOH in NiMesh [52,70]. For NiNPs/NiM and $Fe_{2.5}$@NiNPs/NiM, a component attributed to β-NiOOH (Ni^{2+}/Ni^{3+}) was also detected. This phase is commonly regarded as a precursor to the more catalytically active γ-NiOOH [89–91].

Post-catalytic XPS analysis (after 6 h at 1.7 V vs. RHE) revealed significant spectral changes (Fig. 12b,d,f). The metallic Ni signal decreased in all samples and was completely absent in $Fe_{2.5}$@NiNPs/NiM, indicating full surface oxidation. Additionally, a shift of the Ni $2p_{3/2}$ main peak from 855.6 eV in NiMesh to 856.0 eV in $Fe_{2.5}$@NiNPs/NiM suggests the formation of higher oxidation state Ni^{3+}/Ni^{4+} species [28,71,72]. Notably, β-NiOOH features persisted in NiMesh and NiNPs/NiM but disappeared in the Fe-containing catalyst in gain of $Ni(OH)_2$ species, indicating a more complete and efficient transformation from $Ni(OH)_2$ to the catalytically active phase γ-NiOOH in the presence of Fe [33]. These changes can be correlated with the higher catalytic activity of $Fe_{2.5}$@NiNPs/NiM compared to NiNPs/NiM and NiMesh.

3.5. Full-cell 5 cm² AEM water electrolyser performance

To assess the practical applicability of the $Fe_{5.8}$@NiNPs/NiM electrode, having the best Tafel slope value while maintaining a low overpotential, we extended our investigation beyond the conventional three-

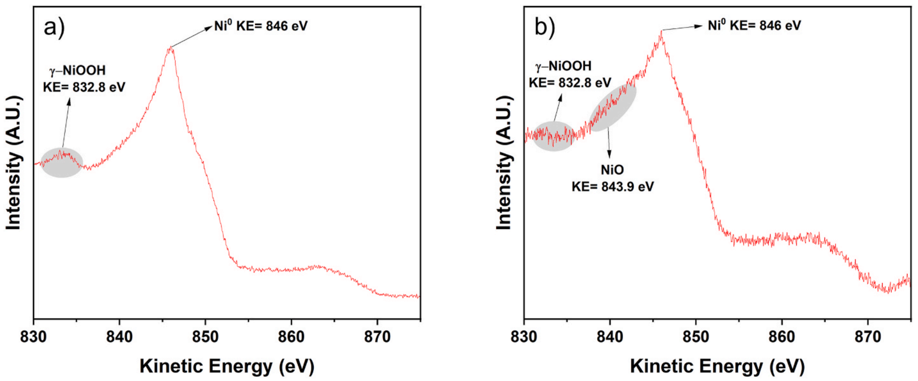

Fig. 11. a) Ni LMM spectra of pre-catalytic NiMesh and b) Ni LMM spectra of pre-catalytic $Fe_{2.5}$@NiNPs/NiM.

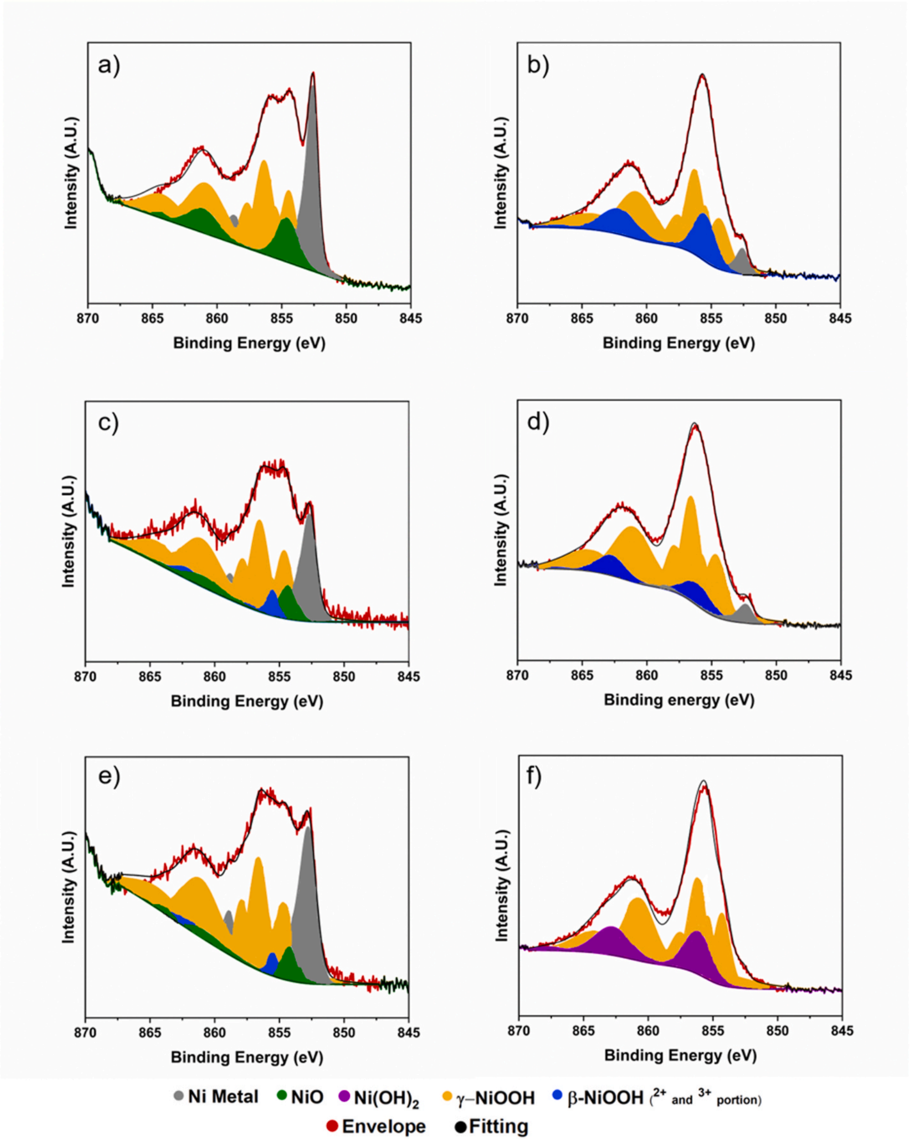

Fig. 12. XPS spectra of Ni $2p_{3/2}$ region from a) Pre-cataytic NiMesh, b) Post-cataytic NiMesh, c) Pre-cataytic NiNPs/NiM, d) Post-cataytic NiNPs/NiM, e) Pre-cataytic $Fe_{2.5}$@NiNPs/NiM and f) Post-cataytic $Fe_{2.5}$@NiNPs/NiM.

electrode set up and evaluated its performance in a full-cell anion exchange membrane water electrolyser (AEMWE). The electrochemical activity of Fe-modified electrode was directly compared to that of pristine NiMesh under identical operating conditions. As shown in the polarization curves of freshly assembled cells, the $Fe_{5.8}$@NiNPs/NiM electrode demonstrated a pronounced improvement in cell performance, reaching a current density of 740 mA/cm^2 at 2.2 V, while the unmodified NiMesh achieved only 305 mA/cm^2 under the same conditions

(Fig. 13). These results are consistent with the catalytic enhancements observed in the three-electrode measurements, confirming the superior intrinsic activity of the Fe-modified catalysts and their effectiveness in realistic electrolyser configurations.

To assess the long-term stability of the $Fe_{5.8}$@NiNPs/NiM electrode under practical operating conditions, potentiostatic electrolysis was carried out at a constant cell voltage of 2.0 V over a period of 72 h. Polarization curves were recorded at 24 h intervals to monitor performance evolution. After the first 24 h, an activation effect was observed, with the current density increasing to a peak value of 930 mA/cm^2. However, after 48 h, a slight decline in performance was noted, with the current density decreasing to 904 mA/cm^2, corresponding to 3.5 % reduction. After 72 h of continuous operation, the final current density was 870 mA/cm^2, indicating a total performance loss of approximately 7 %. Fig. 14 presents the time dependent polarization curves, revealing a relatively low degradation rate of approximately 0.1 % h^{-1}. This degradation rate confirms the need for improvement in terms of operational durability of $Fe_{5.8}$@NiNPs/NiM catalyst for further development in AEM electrolyser systems.

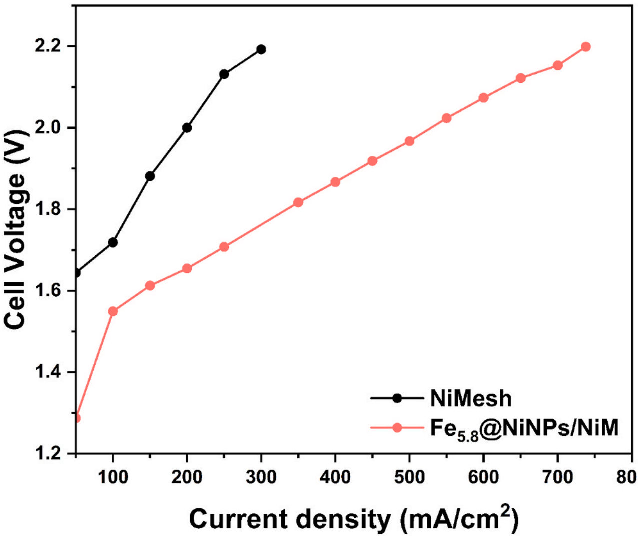

Fig. 13. Polarization curve of as prepared NiMesh and Fe5.8@NiNPs/NiM.

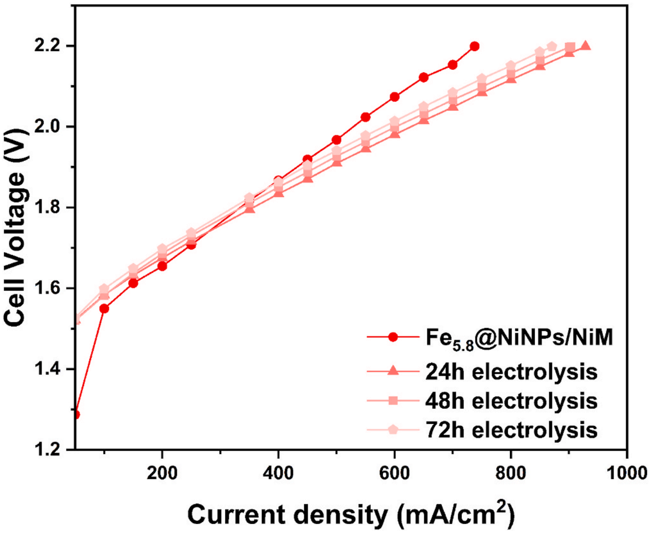

Fig. 14. Polarization curve evolution after 24 h, 48 h and 72 h of electrolysis at 2 V.

4. Conclusions

The improvement of Ni-based catalysts through Fe decoration for alkaline water electrolysis is well-established. However, conventional synthesis methods often yield alloyed bimetallic nanoparticles with poorly defined surface compositions, complicating the analysis of surface-specific effects. In this work, we developed a controlled synthetic approach through magnetic induction that enables selective Fe nucleation on the surface of NiNPs, efficiently preventing homonucleation and allowing precise control over surface Fe–Ni ratios. This proof of concept can be adapted to a huge variety of organometallic precursors and heating agents opening new synthetical routes increasing the control over catalysts prepared for several applications.

Three $Fe_{wt\%}$@NiNPs materials with Fe loadings of 2.5 wt%, 5.8 wt%, and 11 wt% were synthesized, characterized, and evaluated under various electrocatalytic conditions. The results demonstrated a strong dependence of electrocatalytic behaviour on both the Fe/Ni surface ratio and the Ni surface coverage. When $Fe_{wt\%}$@NiNPs were used as the sole active material, performance varied significantly with Fe content. However, when supported on an electrochemically active NiMesh, additional synergistic effects arise from the interaction of $Fe_{wt\%}$@NiNPs with the NiMesh as the Fe present in the surface of $Fe_{wt\%}$@NiNPs comes in contact with the Ni from the NiMesh.

Furthermore, stability assessments revealed that higher Fe content correlates with increased degradation rates, likely due to weaker adhesion when the catalysts were applied via spray coating on to the NiMesh support compared to the deposited $Fe_{wt\%}$@NiNPs/NiM materials. These findings highlight the importance of precise surface composition control and material integration strategies to fully harness the synergistic between Fe and Ni, thereby optimizing both the activity and durability of the electrocatalysts.

Finally, $Fe_{5.8}$@NiNPs/NiM material was successfully tested in a full-cell AEMWE displaying a maximum current density of 930 mA/cm^2 with a performance decrease of ~0.1 % h^{-1} over 72h of continuous electrolysis at 2.0 V. Demonstrating the adaptability of the synthetical procedure upon scaling up materials for catalysts testing from three-electrode systems up to full-cell AEMWEs.

CRediT authorship contribution statement

David Domingo Huguet: Writing – original draft, Visualization, Validation, Methodology, Investigation, Formal analysis, Data curation, Conceptualization. **Víctor Varela-Izquierdo:** Writing – review & editing, Supervision, Investigation, Conceptualization. **Jaime Cervera Martin:** Writing – review & editing, Methodology, Investigation, Conceptualization. **Bruno Chaudret:** Writing – review & editing, Supervision, Resources, Conceptualization. **Katerina Soulantica:** Writing – review & editing, Supervision. **Daniel Ruano Sánchez:** Investigation, Data curation. **Miriam Díaz de los Bernardos Sanchez:** Writing – review & editing, Supervision, Resources, Project administration, Investigation, Funding acquisition, Conceptualization. **Cyril Godard:** Writing – review & editing, Supervision, Resources, Project administration, Funding acquisition, Conceptualization.

Declaration of competing interest

The authors declare that they have no known competing financial interests or personal relationships that could have appeared to influence the work reported in this paper.

5. Acknowledgements

This work was financially supported by the Ministerio de Ciencia, Innovación y Universidades through the project PID2023-147292OB-I00 (MICIU/AEI/10.13039/501100011033) and the Generalitat de Catalunya through the funding grant ACCIÓ-Eurecat (Project TRAÇA-

GreenH2) in which D.D. is a fellow of Eurecat's "Vicente López" PhD grant program and project 2021SGR00163. V.V.I. and B.C. are grateful to the French State aid managed by the Agence Nationale de la Recherche under France 2030 plan, bearing the reference code ANR-22-PESP-0010: Projet ciblé "POWERCO2" within the PEPR project SPLEEN. J.C.M. thanks the IFP Energies Nouvelles for financial support. HRTEM equipment was partially funded by the operative program FEDER Catalunya 2014–2020 (IU16-015844). D.R. and URV would also like to thank the project EQC2021-007785-P, awarded by the Ministry of Science and Innovation, and funded by the European Union (NextGeneration), for the total funding of the XPS system (ProvenX-NAP from SPECS) at the SRCiT of the URV.

Appendix A. Supplementary data

Supplementary data to this article can be found online at https://doi.org/10.1016/j.ijhydene.2025.151868.

References

[1] Dawood F, Anda M, Shafiullah GM. Hydrogen production for energy: an overview. Int J Hydrogen Energy 2020;45:3847–69. https://doi.org/10.1016/j.ijhydene.2019.12.059.

[2] Sen R, Das S, Nath A, Maharana P, Kar P, Verpoort F, et al. Electrocatalytic water oxidation: an overview with an example of translation from lab to market. Front Chem 2022;10:1–24. https://doi.org/10.3389/fchem.2022.861604.

[3] Jin L, Nogueira Nakashima R, Comodi G, Frandsen HL. Alkaline electrolysis for green hydrogen production: a novel, simple model for thermo-electrochemical coupled system analysis. Appl Therm Eng 2025;262:125154. https://doi.org/10.1016/J.APPLTHERMALENG.2024.125154.

[4] Dash S, K AS, S J, D VHW, D E, Surapraraju SK, et al. Advances in green hydrogen production through alkaline water electrolysis: a comprehensive review. Int J Hydrogen Energy 2024;83:614–29. https://doi.org/10.1016/J.IJHYDENE.2024.08.157.

[5] Muthiah M, Elnashar M, Afzal W, Tan H. Safety assessment of hydrogen production using alkaline water electrolysis. Int J Hydrogen Energy 2024;84:803–21. https://doi.org/10.1016/J.IJHYDENE.2024.08.237.

[6] Guo Y, Li G, Zhou J, Liu Y. Comparison between hydrogen production by alkaline water electrolysis and hydrogen production by PEM electrolysis. IOP Conf Ser Earth Environ Sci 2019;371. https://doi.org/10.1088/1755-1315/371/4/042022.

[7] Ehlers JC, Feidenhans'l AA, Therkildsen KT, Larrazábal GO. Affordable green hydrogen from alkaline water electrolysis: key research needs from an industrial perspective. ACS Energy Lett 2023;8:1502–9. https://doi.org/10.1021/acsenergylett.2c02897.

[8] Faqeeh AH, Symes MD. Zero-gap bipolar membrane water electrolyzers: principles, challenges and practical insights. Electrochim Acta 2024;493:144345. https://doi.org/10.1016/J.ELECTACTA.2024.144345.

[9] Wang T, Cao X, Jiao L. PEM water electrolysis for hydrogen production: fundamentals, advances, and prospects. Carbon Neutrality 2022;1. https://doi.org/10.1007/S43979-022-00022-8.

[10] Shiva Kumar S, Himabindu V. Hydrogen production by PEM water electrolysis – a review. Mater Sci Energy Technol 2019;2:442–54. https://doi.org/10.1016/J.MSET.2019.03.002.

[11] Carmo M, Fritz DL, Mergel J, Stolten D. A comprehensive review on PEM water electrolysis. Int J Hydrogen Energy 2013;38:4901–34. https://doi.org/10.1016/J.IJHYDENE.2013.01.151.

[12] Shi Y, Min X, Lu Z, Yan C. Highly efficient PEM water electrolyser with noble metal loading less than 0.2 Mg/cm2. ECS Meet Abstr 2020. https://doi.org/10.1149/MA2020-01371571MTGABS. MA2020-01:1571.

[13] Wijaya GHA, Im KS, Nam SY. Advancements in commercial anion exchange membranes: a review of membrane properties in water electrolysis applications. Desalin Water Treat 2024;320:100605. https://doi.org/10.1016/J.DWT.2024.100605.

[14] Ferriday TB, Sampathkumar SN, Middleton PH, Kolhe ML, Van Herle J. A review of membrane electrode assemblies for the anion exchange membrane water electrolyser: perspective on activity and stability. Int J Energy Res 2024;2024:7856850. https://doi.org/10.1155/2024/7856850.

[15] Liu Y, Song Q, Xu T, Kong Q, He G, Sun H, et al. Novel large-scale integrated non-precious metal electrodes for efficient and stable oxygen evolution reaction at high current density in 2.5 kW anion exchange membrane water electrolysis. Appl Catal B Environ 2025;363:124811. https://doi.org/10.1016/j.apcatb.2024.124811.

[16] Miller HA, Bouzek K, Hnat J, Loos S, Bernäcker CI, Weißgärber T, et al. Green hydrogen from anion exchange membrane water electrolysis: a review of recent developments in critical materials and operating conditions. Sustain Energy Fuels 2020;4:2114–33. https://doi.org/10.1039/C9SE01240K.

[17] Matsumoto Y, Sato E. Electrocatalytic properties of transition metal oxides for oxygen evolution reaction. Mater Chem Phys 1986;14:397–426. https://doi.org/10.1016/0254-0584(86)90045-3.

[18] Liu S, Wei Y, Wang M, Shen Y. The future of alkaline water splitting from the perspective of electrocatalysts-seizing today's opportunities. https://doi.org/10.1016/j.ccr.2024.216190; 2024.

[19] Negahdar L, Zeng F, Palkovits S, Broicher C, Palkovits R. Mechanistic aspects of the electrocatalytic oxygen evolution reaction over Ni−Co oxides. Chemelectrochem 2019;6:5588–95. https://doi.org/10.1002/celc.201901265.

[20] Zhang N, Chai Y. Lattice oxygen redox chemistry in solid-state electrocatalysts for water oxidation. Energy Environ Sci 2021;14:4647–71. https://doi.org/10.1039/d1ee01277k.

[21] Boppella R, Tan J, Yun J, Manorama SV, Moon J. Anion-mediated transition metal electrocatalysts for efficient water electrolysis: recent advances and future perspectives. Coord Chem Rev 2021;427:213552. https://doi.org/10.1016/J.CCR.2020.213552.

[22] Wen N, Jiao X, Xia Y, Chen D. Electrocatalysts for the oxygen evolution reaction: mechanism, innovative strategies, and beyond. Mater Chem Front 2023;7:4833. https://doi.org/10.1039/d3qm00423f.

[23] Raveendran A, Chandran M, Dhanusuraman R. A comprehensive review on the electrochemical parameters and recent material development of electrochemical water splitting electrocatalysts. RSC Adv 2023;13:3843–76. https://doi.org/10.1039/D2RA07642J.

[24] Luo X, Tan X, Ji P, Chen L, Yu J, Mu S. Surface reconstruction-derived heterostructures for electrochemical water splitting. https://doi.org/10.1016/j.enchem.2022.100091; 2022.

[25] Yu M, Budiyanto E, Tüysüz H. Principles of water electrolysis and recent progress in Cobalt-, Nickel-, and iron-based oxides for the oxygen evolution reaction. Angew Chemie - Int Ed 2022;61. https://doi.org/10.1002/anie.202103824.

[26] Yang L, Liu Z, Zhu S, Feng L, Xing W. Ni-based layered double hydroxide catalysts for oxygen evolution reaction. Mater Today Phys 2021;16. https://doi.org/10.1016/j.mtphys.2020.100292.

[27] Singh A, Chang SLY, Hocking RK, Bach U, Spiccia L. Highly active nickel oxide water oxidation catalysts deposited from molecular complexes. Energy Environ Sci 2013;6:579–86. https://doi.org/10.1039/c2ee23862d.

[28] Friebel D, Louie MW, Bajdich M, Sanwald KE, Cai Y, Wise AM, et al. Identification of highly active Fe sites in (Ni,Fe)OOH for electrocatalytic water splitting. J Am Chem Soc 2015;137:1305–13. https://doi.org/10.1021/JA511559D/SUPPL_FILE/JA511559D_SI_001.PDF.

[29] Cai Z, Liang J, Li Z, Yan T, Yang C, Sun S, et al. Stabilizing NiFe sites by high-dispersity of nanosized and anionic Cr species toward durable seawater oxidation. Nat Commun 2024;15:1–12. https://doi.org/10.1038/s41467-024-51130-1. 2024 151.

[30] Gong M, Li Y, Wang H, Liang Y, Wu JZ, Zhou J, et al. An advanced Ni-Fe layered double hydroxide electrocatalyst for water oxidation. J Am Chem Soc 2013;135:8452–5. https://doi.org/10.1021/ja4027715.

[31] Sohel A, Kovilakath MSN, Gogoi PJ, Ansari H, Phukan P, Bag S, et al. Mechanistic insights into the stabilization of in situ formed γ-NiOOH species on Ni60Nb40 nanoglass for effective urea electro-oxidation. Small 2024;20:2405160. https://doi.org/10.1002/SMLL.202405160.

[32] He Z Da, Tesch R, Eslamibidgoli MJ, Eikerling MH, Kowalski PM. Low-spin state of Fe in Fe-doped NiOOH electrocatalysts. Nat Commun 2023;141:1–9. https://doi.org/10.1038/s41467-023-38978-5. 2023;14.

[33] Chen KL, Chou YH, Lin TJ, Cheng MJ, Hsiao PK, Pu YC, et al. Real-time monitoring of Fe-Induced stable γ-NiOOH in binder-free FeNi MOF electrocatalysts for enhanced oxygen evolution. Small 2025:2501142. https://doi.org/10.1002/SMLL.202501142.

[34] Li Z, Wang D, Kang H, Shi Z, Hu X, Sun H, et al. Atomic cation and anion co-vacancy defects boosted the oxide path mechanism of the oxygen evolution reaction on NiFeAl-layered double hydroxide. J Mater Chem A 2024. https://doi.org/10.1039/d4ta05839a.

[35] Li X, Wang M, Fu J, Lu F, Li Z, Wang G. Sulfurized NiFe2O4 electrocatalyst with in situ formed Fe-NiOOH nanoparticles to realize industrial-level oxygen evolution. Small 2024;20:1–8. https://doi.org/10.1002/smll.202310040.

[36] Qu H, Ma Y, Li X, Duan Y, Li Y, Liu F, et al. Ternary alloy (FeCoNi) nanoparticles supported on hollow porous carbon with defects for enhanced oxygen evolution reaction. J Colloid Interface Sci 2023;645:107–14. https://doi.org/10.1016/j.jcis.2023.04.122.

[37] Garcés-Pineda FA, Yu J, Mesa CA, Plana-Ruiz S, Ruano D, Liang Y, et al. Operando evidence on the chirality-enhanced oxygen evolution reaction in intrinsically chiral electrocatalysts. Chem Sci 2025. https://doi.org/10.1039/d4sc07927b.

[38] Ciambriello L, Alessandri I, Gavioli L, Vassalini I. NiFe catalysts for oxygen evolution reaction: is there an optimal thickness for generating a dynamically stable active interface? ChemCatChem 2024;16. https://doi.org/10.1002/cctc.202400286.

[39] Varghese NK, Mkrtchian E, Singh A, Savio L, Boccia M, Marzocchi V, et al. NiFe on CeO2, TiO2, and ZrO2 supports as efficient oxygen evolution reaction catalysts in alkaline media. ACS Appl Energy Mater 2025. https://doi.org/10.1021/acsaem.4c03268.

[40] Moses AJ. Eddy current losses in soft magnetic materials. Wiley Encycl Electr Electron Eng 2015:1–22. https://doi.org/10.1002/047134608X.W4531.PUB2.

[41] Margeat O, Ciuculescu D, Lecante P, Respaud M, Amiens C, Chaudret B. NiFe nanoparticles: a soft magnetic material? Small 2007;3:451–8. https://doi.org/10.1002/smll.200600329.

[42] Mazarío J, Ghosh S, Varela-Izquierdo V, Martínez-Prieto LM, Chaudret B. Magnetic nanoparticles and radio frequency induction: from specific heating to magnetically induced catalysis. ChemCatChem 2024:202400683. https://doi.org/10.1002/cctc.202400683.

[43] Quiroga-Suavita F, Varela-Izquierdo V, Hungria T, Alloyeau D, Ratel-Ramond N, Cayez S, et al. Icosahedra CoPd bimetallic nanoparticles for magnetically induced aromatic ketone hydrodeoxygenation. Chem Mater 2025;37:2762–71. https://doi.org/10.1021/ACS.CHEMMATER.4C03359/SUPPL_FILE/CM4C03359_SI_001.PDF.

[44] Varela-Izquierdo V, Mustieles-Marín I, Fazzini PF, Mencía G, Guelen S, Rachet R, et al. Magnetically induced amination of alcohols using MNi@Cu (M=Fe, co) nanoparticles as catalysts. Angew Chemie Int Ed 2024;63:e202412421. https://doi.org/10.1002/ANIE.202412421.

[45] Raya-Barón Á, Ghosh S, Mazarío J, Varela-Izquierdo V, Fazzini PF, Tricard S, et al. Induction heating: an efficient methodology for the synthesis of functional core–shell nanoparticles. Mater Horizons 2023;10:4952–9. https://doi.org/10.1039/D3MH00908D.

[46] Niether C, Faure S, Bordet A, Deseure J, Chatenet M, Carrey J, et al. Improved water electrolysis using magnetic heating of FeC–Ni core–shell nanoparticles. Nat Energy 2018;36:476–83. https://doi.org/10.1038/S41560-018-0132-1. 2018;3.

[47] Gatard V, De Masi D, Chattot R, Marin IM, Revert JMA, Fazzini PF, et al. FeNi3 and Ni-Based nanoparticles as electrocatalysts for magnetically enhanced alkaline water electrolysis. Electrocatalysis 2021;11:567–77. https://doi.org/10.1007/S12678-020-00616-9/FIGURES/7.

[48] Gatard V, Marin IM, De Masi D, Encinas T, Charlot F, Martin V, et al. Durability of the FeNi 3 @ni material designed for water electrolysis enhanced by high frequency alternating magnetic field. Cite This ACS Appl Energy Mater 2022;2022:7048. https://doi.org/10.1021/acsaem.2c00663.

[49] El-Sayed HA, Weiß A, Olbrich LF, Putro GP, Gasteiger HA. OER catalyst stability investigation using RDE technique: a stability measure or an artifact? J Electrochem Soc 2019;166:F458–64. https://doi.org/10.1149/2.0301908jes.

[50] An H, Park W, Shin H, Chung DY. Recommended practice for measurement and evaluation of oxygen evolution reaction electrocatalysis. EcoMat 2024;6:1–22. https://doi.org/10.1002/eom2.12486.

[51] Volk EK, Kreider ME, Kwon S, Alia SM. Recent progress in understanding the catalyst layer in anion exchange membrane electrolyzers-durability, utilization, and. integration 2024;2:109. https://doi.org/10.1039/d3ey00193h.

[52] Palmas S, Rodriguez J, Mais L, Mascia M, Herrando MC, Vacca A. Anion exchange membrane: a valuable perspective in emerging technologies of low temperature water electrolysis. Curr Opin Electrochem 2023;37:101178. https://doi.org/10.1016/J.COELEC.2022.101178.

[53] Rietveld HM. A profile refinement method for nuclear and magnetic structures. J Appl Crystallogr 1969;2:65–71. https://doi.org/10.1107/S0021889869006558.

[54] Coelho AA. Optimum Levenberg–Marquardt constant determination for nonlinear least-squares. J Appl Crystallogr 2018;51:428–35. https://doi.org/10.1107/S1600576718001784/PO5119SUP24.TXT.

[55] Cheary RW, Coelho AA, Cline JP. Fundamental parameters line profile fitting in laboratory diffractometers. J Res Natl Inst Stand Technol 2004;109:1–25. https://doi.org/10.6028/JRES.109.002.

[56] Hill RJ, Howard CJ. Quantitative phase analysis from neutron powder diffraction data using the Rietveld method. J Appl Crystallogr 1987;20:467–74. https://doi.org/10.1107/S0021889887086199.

[57] Balzar D. Voight function model in diffraction-line broadening analysis. 1999. Chap. 7.

[58] Bordet A, Lacroix LM, Fazzini PF, Carrey J, Soulantica K, Chaudret B. Magnetically induced continuous CO2Hydrogenation using composite iron carbide nanoparticles of exceptionally high heating power. Angew Chemie - Int Ed 2016;55:15894–8. https://doi.org/10.1002/anie.201609477.

[59] Grey LH, Nie HY, Biesinger MC. Defining the nature of adventitious carbon and improving its merit as a charge correction reference for XPS. Appl Surf Sci 2024;653:159319. https://doi.org/10.1016/j.apsusc.2024.159319.

[60] Payne BP, Biesinger MC, McIntyre NS. Use of oxygen/nickel ratios in the XPS characterisation of oxide phases on nickel metal and nickel alloy surfaces. J Electron Spectros Relat Phenomena 2012;185:159–66. https://doi.org/10.1016/j.elspec.2012.06.008.

[61] Biesinger MC. Accessing the robustness of adventitious carbon for charge referencing (correction) purposes in XPS analysis: insights from a multi-user facility data review. Appl Surf Sci 2022;597:153681. https://doi.org/10.1016/j.apsusc.2022.153681.

[62] Biesinger MC, Payne BP, Grosvenor AP, Lau LWM, Gerson AR, Smart RSC. Resolving surface chemical states in XPS analysis of first row transition metals, oxides and hydroxides: cr, Mn, Fe, Co and Ni. Appl Surf Sci 2011;257:2717–30. https://doi.org/10.1016/j.apsusc.2010.10.051.

[63] Hughes AE, Easton CD, Gengenbach TR, Biesinger MC, Laleh M. Interpretation of complex x-ray photoelectron peak shapes. I. Case study of Fe 2p3/2 spectra. J Vac Sci Technol A 2024;42. https://doi.org/10.1116/6.0003804.

[64] Bard AJ, Faulkner LR, White HS. Electrochemical methods : fundamentals and applications. Third edit. Hoboken, NJ SE - Liii, 1044 Pàgines ; 24 Cm. Wiley; 2022.

[65] Motealleh B, Liu Z, Masel RI, Sculley JP, Ni ZR, Meroueh L. Next-generation anion exchange membrane water electrolyzers operating for commercially relevant lifetimes. https://doi.org/10.1016/j.ijhydene.2020.10.244; 2020.

[66] Pearson WB. A handbook of lattice spacings and structures of metals and alloys, vol. II. Pergamon Press LTD.; 1964.

[67] Kabekkodu SN, Dosen A, Blanton TN. PDF-5+: a comprehensive powder diffraction File$^{\text{TM}}$ for materials characterization. Powder Diffr 2024;39:47–59. https://doi.org/10.1017/S0885715624000150.

[68] Meffre A, Mehdaoui B, Connord V, Carrey J, Fazzini PF, Lachaize S, et al. Complex nano-objects displaying both magnetic and catalytic properties: a proof of concept for magnetically induced heterogeneous catalysis. Nano Lett 2015;15:3241–8. https://doi.org/10.1021/ACS.NANOLETT.5B00446/SUPPL_FILE/NL5B00446_SI_001.PDF.

[69] Asensio JM, Marbaix J, Mille N, Lacroix LM, Soulantica K, Fazzini PF, et al. To heat or not to heat: a study of the performances of iron carbide nanoparticles in magnetic heating. Nanoscale 2019;11:5402–11. https://doi.org/10.1039/C8NR10235J.

[70] Wang S, Zhang J, Gharbi O, Vivier V, Gao M, Orazem ME. Electrochemical impedance spectroscopy. Nat Rev Methods Prim 2021;1. https://doi.org/10.1038/s43586-021-00039-w.

[71] Lu B, Huang H, Dong XL, Zhang XF, Lei JP, Sun JP, et al. Influence of alloy components on electromagnetic characteristics of core/shell-type Fe-Ni nanoparticles. J Appl Phys 2008;104. https://doi.org/10.1063/1.3040006/146826.

[72] Li XG, Chiba A, Takahashi S. Preparation and magnetic properties of ultrafine particles of FeNi alloys. J Magn Magn Mater 1997;170:339–45. https://doi.org/10.1016/S0304-8853(97)00039-5.

[73] El-Gendy AA, Ibrahim EMM, Khavrus VO, Krupskaya Y, Hampel S, Leonhardt A, et al. The synthesis of carbon coated Fe, Co and Ni nanoparticles and an examination of their magnetic properties. Carbon N Y 2009;47:2821–8. https://doi.org/10.1016/J.CARBON.2009.06.025.

[74] Dijith KS, Aiswarya R, Praveen M, Pillai S, Surendran KP. Polyol derived Ni and NiFe alloys for effective shielding of electromagnetic interference. Mater Chem Front 2018;2:1829–41. https://doi.org/10.1039/C8QM00264A.

[75] De Masi D, Asensio JM, Fazzini PF, Lacroix LM, Chaudret B. Engineering iron–nickel nanoparticles for magnetically induced CO2 methanation in continuous flow. Angew Chemie - Int Ed 2020;59:6187–91. https://doi.org/10.1002/anie.201913865.

[76] Doyle RL, Godwin IJ, Brandon MP, Lyons MEG. Redox and electrochemical water splitting catalytic properties of hydrated metal oxide modified electrodes. Phys Chem Chem Phys 2013;15:13737–83. https://doi.org/10.1039/C3CP51213D.

[77] Kim B, Kabiraz MK, Lee J, Choi C, Baik H, Jung Y, et al. Vertical-crystalline Fe-doped β-Ni oxyhydroxides for highly active and stable oxygen evolution reaction. Matter 2021;4:3585–604. https://doi.org/10.1016/J.MATT.2021.09.003.

[78] Xu Q, Zhang L, Zhang J, Wang J, Hu Y, Jiang H, et al. Anion exchange membrane water electrolyzer: electrode design, lab-scaled testing system and performance evaluation. EnergyChem 2022;4:100087. https://doi.org/10.1016/j.enchem.2022.100087.

[79] Chen W, Xiang Q, Peng T, Song C, Shang W, Deng T, et al. Reconsidering the benchmarking evaluation of catalytic activity in oxygen reduction reaction. iScience 2020;23:101532. https://doi.org/10.1016/J.ISCI.2020.101532.

[80] Trotochaud L, Young SL, Ranney JK, Boettcher SW. Nickel-iron oxyhydroxide oxygen-evolution electrocatalysts: the role of intentional and incidental iron incorporation. J Am Chem Soc 2014;136:6744–53. https://doi.org/10.1021/ja502379c.

[81] Wang Y, Han Y, Yan K, Huang Y, Zhang M, Lai X, et al. Effects of Fe on electrocatalytic oxygen evolution reaction activity for CoFe layered double hydroxide nanosheets. J Alloys Compd 2022;903:163994. https://doi.org/10.1016/j.jallcom.2022.163994.

[82] Anantharaj S, Kundu S, Noda S. "The Fe effect": a review unveiling the critical roles of Fe in enhancing OER activity of Ni and Co based catalysts. Nano Energy 2021;80. https://doi.org/10.1016/j.nanoen.2020.105514.

[83] Bennettand H, Wiley GJO, Benninghoven A, Janssen KTF, Tumpner J, Wer HW. High resolution XPS of organic polymers: the scienta ESCA300 database (Beamson, G.; Briggs, D.). J Chem Educ 1993;70:A25. https://doi.org/10.1021/ED070PA25.5.

[84] Fluorine | XPS periodic table | thermo fisher scientific - ES n.d. https://www.thermofisher.com/es/es/home/materials-science/learning-center/periodic-table/halogen/fluorine.html. [Accessed 6 May 2025].

[85] Morgan DJ. Comments on the XPS Analysis of Carbon Materials. C7:51. 2021. https://doi.org/10.3390/c7030051.

[86] X-ray photoelectron spectroscopy (XPS) reference pages: potassium n.d. http://www.xpsfitting.com/2020/02/potassium.html (accessed May 6, 2025).

[87] Biesinger MC, Lau LWM, Gerson AR, Smart RSC. The role of the Auger parameter in XPS studies of nickel metal, halides and oxides. Phys Chem Chem Phys 2012;14:2434–42. https://doi.org/10.1039/c2cp22419d.

[88] Grosvenor AP, Biesinger MC, Smart RSC, McIntyre NS. New interpretations of XPS spectra of nickel metal and oxides. Surf Sci 2006;600:1771–9. https://doi.org/10.1016/j.susc.2006.01.041.

[89] Gallenberger J, Moreno Fernández H, Alkemper A, Li M, Tian C, Kaiser B, et al. Stability and decomposition pathways of the NiOOH OER active phase of NiOx electrocatalysts at open circuit potential traced by ex situ and in situ spectroscopies. Catal Sci Technol 2023;13:4693–700. https://doi.org/10.1039/d3cy00674c.

[90] Haghverdi Khamene S, van Helvoirt C, Tsampas MN, Creatore M. Electrochemical activation of atomic-layer-deposited nickel oxide for water oxidation. J Phys Chem C 2023;127:22570–82. https://doi.org/10.1021/acs.jpcc.3c05002.

[91] Menezes PW, Yao S, Beltrán-Suito R, Hausmann JN, Menezes PV, Driess M. Facile access to an active γ-NiOOH electrocatalyst for durable water oxidation derived from an intermetallic nickel germanide precursor. Angew Chemie - Int Ed 2021;60:4640–7. https://doi.org/10.1002/anie.202014331.